Separation efficiency of flat- and domed-roof cyclones in high-pressure polypropylene production using computational fluid dynamics

Hanh Thi Hong Bui, Son Ich Ngo, and Young-Il Lim†

Center of Sustainable Process Engineering (CoSPE), Department of Chemical Engineering,
Hankyong National University, Jungang-ro 327, Anseong-si, Gyeonggi-do 17579, Korea
(*Received 7 February 2023 • Revised 30 May 2023 • Accepted 1 June 2023*)

Abstract−Separation efficiency of flat- and domed-roof cyclones was investigated in a polypropylene (PP) production process at 20 bar and 80 °C, using computational fluid dynamics (CFD) coupled with the Reynolds stress model for gas turbulence and a discrete random walk model for particles. The geometry of the domed-roof cyclone was based on a high-efficiency Stairmand cyclone and the ASME standard for high-pressure vessels. The meshing strategy and CFD model validation of the cyclones were performed systematically. At an inlet velocity of 20 m/s and atmospheric pressure, the fractional separation efficiency of the domed-roof cyclone was 1.5% higher than that of the flat-roof cyclone in an air-$CaCO_3$ system for particle sizes ranging from 0.1 to 100 µm. Under the high-pressure operating conditions of the domed-roof cyclone, the diameter (D_e) of the vortex finder was selected as 40% of the cyclone barrel diameter (D), maintaining its high separation efficiency and moderate pressure drop. The optimized domed-roof cyclone achieved an 8.4% higher mean fractional separation efficiency and a 6.4% lower pressure drop compared to a standard flat-roof cyclone for PP particles from 1 to 40 µm. The CFD result provides a useful guide for designing a high-efficiency domed-roof cyclone at high pressures.

Keywords: Domed-roof Cyclone, Polypropylene Particles, Separation Efficiency, Computational Fluid Dynamics (CFD), Eulerian-Lagrangian Method

INTRODUCTION

Cyclones have been successfully employed in a variety of chemical processes to separate solid particles from transporting gas flows because of their low cost, simple structure without moving parts, high separation efficiency, and flexibility in processing materials and operating conditions [1]. Highly efficient Stairmand industrial cyclones are available for most chemical processes, such as dust collection [2], fluid catalytic cracking (FCC) [3], and mineral recovery [1]. However, advanced design of cyclones is required for processes with particle deposition on the surface [3], fluctuating inlet velocity [4], phase change [5], high pressure in natural gas stations [6] and polymerization [7,8].

Considering solid particle properties, Song et al. [3] investigated FCC particle deposition on the outer surface of a vortex finder in a cyclone at high gas velocity and temperature. The vortex power for different vortex finder heights was examined for a cyclone with an oscillating inlet flow from a combustion engine [4]. Jiang et al. [5] reported a long electrostatic cyclone demister for removing small droplets.

In the commercialized gas-phase propylene (PP) polymerization process [8-10], such as the Unipol process of DOW chemicals, the Spheriline process of LyondellBasell, Evolue of Mitsui, and the Novolen process of Lummus Technology, a cyclone is usually placed after the fluidized-bed reactor to eliminate fine particles from the recycle stream [7,8]. As the PP polymerization process is commonly operated at high pressures ranging from 10 to 35 bar, a domed-roof barrel cyclone is mechanically more suitable than a flat-roof cyclone [1,6]. However, replacing a flat roof with a domed roof may deteriorate separation efficiency [1].

Along with the growth of computational capability and the prediction accuracy of models, computational fluid dynamics (CFD) has been widely applied to chemical processes to improve geometry design and process performance [11]. Elsayed and Lacor [12] summarized a numerical procedure for modeling a cyclone, including model selection, solver setting, numerical method, boundary conditions, and the grid convergence index (GCI) method.

The Eulerian-Eulerian (EE) and Eulerian-Lagrangian (EL) methods are the two main CFD approaches for gas and solid flows. Because the EE method treats both flows as a continuous phase, each domain representing a single particle size is considered an individual pseudo-fluid state of the solid-gas mixture phase. The EE method, coupled with the kinetic theory of granular flow, is commonly used for modeling multiphase flows with a single particle size and a high volume fraction of solid particles, such as in fluidized-beds [13,14]. The EL method adopts a continuum description and a discrete particle trajectory for gas and solid phases, respectively [3,6,15]. The EL method is preferable to the EE method for modeling cyclones with gas and solid phases, where the volume fraction of the solid particles is relatively small [3,16]. The EL method has been used for most modeling studies on cyclones with a particle volume fraction of less than 10% [2,4-6,12,17-20].

A crucial issue in the CFD simulation of a cyclone is selecting the turbulence model [12,21]. The Reynolds stress model (RSM), which is a Reynolds-averaged Navier-Stokes approach [2,5,6,12,17, 18,22-24] and large eddy simulation (LES) [4,19,20,25] are commonly used to predict swirling and rotational flows accurately. Jang et al. [20] and Shukla et al. [26] concluded that both the RSM and LES showed good agreement with the experimental data. Although LES showed higher accuracy in fluctuating velocity profiles than RSM, the mean flow field of LES was similar to that of RSM [26]. Pandey [27] investigated the performance of cyclones using RSM with an omega-pressure strain sub-model. Shukla [26] and Kaya [28] showed that the linear-pressure strain model for turbulence achieved a high level of agreement compared to experiment data.

The influence of the cyclone geometry on the separation performance was intensively investigated with the aid of CFD. Based on the Stairmand cyclone design, the geometrical improvement of the cyclones was examined under various operating conditions and particle properties. Using three-dimensional (3D) CFD coupled with LES, Elsayed and Lacor [12] reported an insignificant effect of cone-tip diameters on cyclone performance, such as separation efficiency, cut-off diameter, and pressure drop. Wu and Chen [18] evaluated multiple vortex finder designs with different diameters and shapes (contracted and expanded) using 3D CFD with RSM. Zhang et al. [2] clarified the correlation between the structural parameters of vortex finders and the separation performance by adopting a 3D CFD coupled with a discrete phase model (DPM) for the solid phase and RSM. Using 3D CFD with DPM and RSM, Yohana et al. [17] proposed a special vortex finder geometry (called a tapered in-cylinder out) to reduce the cyclone pressure drop by up to 13% while maintaining good separation efficiency.

Research comparing roof or head design of cyclones is scarce [1]. Hoffmann and Stein [1] reported that a domed-roof cyclone impaired separation performance for ambient operating conditions, as mentioned earlier. Based on guidelines from the American Society of Mechanical Engineers (ASME) for high-pressure vessels, Fathizadeh et al. [6] designed a high-pressure cyclone with a domed-roof to improve the separation efficiency over a standard cyclone with a flat-roof. However, the diameter and length of the vortex finder have not been optimized. Furthermore, the reason for the better performance of the domed-roof cyclone is unclear. To date, a high-pressure cyclone with a domed-roof for PP production has not been discussed.

This study aimed to design a domed-roof cyclone suitable for separating fine particles in a PP polymerization process under high pressure using CFD. To accomplish this, an EL method coupled with RSM was used, and the trajectory of the particles was tracked by the DPM. The grid convergence index (GCI) method was adopted to determine the appropriate mesh density of the CFD domain, considering the numerical accuracy and computational cost. The CFD results were then validated against the experimental data obtained from the literature. A Stairmand cyclone with a flat-roof was compared with a domed-roof cyclone in terms of pressure drop and separation efficiency. Hydrodynamics such as pressure drop and gas velocity of domed-roof cyclones for high-pressure PP production process were investigated by changing the vortex finder diameters. Finally, an optimized geometry of the vortex finder was
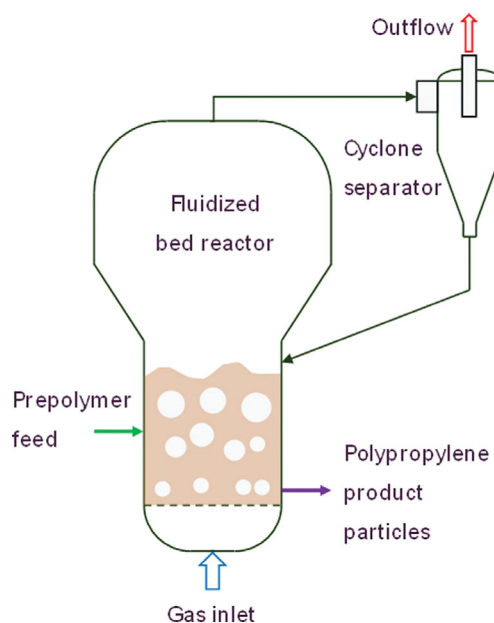

Fig. 1. Schematic diagram of the polypropylene (PP) production process with a fluidized-bed reactor (FBR) and cyclone [7].

proposed for a dome-roof cyclone. This study elucidates how a domed-roof cyclone under high pressure achieves a high separation performance for fine particles.

HIGH-PRESSURE CYCLONE IN POLYPROPYLENE POLYMERIZATION PROCESS

In most fluidized-bed reactors (FBRs), the fluidized state is maintained by an ascending stream of gas, and a cyclone separator is necessary to capture fine particles that pass through the FBRs [7,8]. For the gas-phase polymerization of PP in a fluidized-bed, fine PP particles should be separated and then recycled to the suspension to prevent the escape of fine particles, which may cause the loss of PP and pipeline blocking [7]. The typical operating temperature and pressure were 80 °C and 20 bar [7-9] in the PP production process. Owing to the mechanical strength issue at high temperature and pressure, a domed-roof cyclone was preferred [1,6] based on the Stairmand high-efficiency cyclone design [29].

Fig. 1 shows the PP production process using FBR. The prepolymer particles were prepared in a catalyst reactor and injected into the middle of the FBR [30]. Approximately 80% of the mass of PP particles was entrained in the upper part of the reactor [7]. The cyclone connected to the reactor outlet removed at least 90% of particles with a diameter of 10 μm from the gas flow. The removed particles were recycled into the FBR to continue the polymerization process. PP product particles with a large diameter settled to the bottom of the FBR and were removed [7,30].

MATHEMATICAL MODELING OF CYCLONES

A Stairmand high-efficiency cyclone (D=0.29 m) [29] was used in the numerical study. An EL CFD model was developed to investigate the separation efficiency of cyclones with flat and domed

roofs. The geometry of the domed-roof cyclone with three different vortex finder diameters was examined to determine the optimum diameter of the vortex finder. Mesh density analyses were performed for the highest inlet velocity under the experimental conditions of a flat-roof cyclone [29]. Although many researchers have applied unsteady-state simulation to cyclone separators [19,31,32], steady-state simulation is still useful for evaluating time-averaged quantities, saving computational time [33-35]. In this study, both steady-state and unsteady-state simulations were performed.

1. Computational Fluid Dynamics (CFD) Model

The gas flow in the cyclone was assumed to be isothermal and incompressible. The physical properties and boundary conditions were fixed at a given operating temperature (see Section 3.2). The particles were expected to be spherical. The buoyancy effect on turbulence was neglected because of isothermal conditions. The CFD model is presented in Table 1. Since the energy conservation equation was not included in the governing equations, the effect of heat transfer on the cyclone performance was not considered. In the EL

Table 1. Eulerian-Lagrangian CFD model coupled with the Reynolds stress model (RSM) for turbulence

Name	Mathematical expression	Eq.
Continuity Eq.	$\frac{\partial \overline{u}_i}{\partial x_i} = 0$, i=1, 2, and 3	(T1)
Momentum conservation Eq.	$\frac{\partial \overline{u}_i}{\partial t} + \overline{u}_j \frac{\partial \overline{u}_i}{\partial x_i} = -\frac{1}{\rho}\frac{\partial \overline{P}}{\partial x_i} + \mu \frac{\partial^2 \overline{u}_i}{\partial x_j \partial x_j} - \frac{\partial}{\partial x_j}\rho \overline{u_i' u_j'}$, where $u_i' = u_i - \overline{u}_i$	(T2)
Reynolds stress model	$\frac{\partial}{\partial t}(\rho \overline{u_i' u_j'}) + \frac{\partial}{\partial x_k}(\rho u_k \overline{u_i' u_j'}) = -D_{T,ij} + D_{L,ij} - P_{ij} + \varphi_{ij} - \varepsilon_{ij}$	(T3)
- Turbulent diffusion	$D_{T,ij} = \frac{\partial}{\partial x_k}[\rho \overline{u_i' u_j' u_k'} + \overline{p'(\delta_{kj} u_i' + \delta_{ik} u_j')}] \approx \frac{\partial}{\partial x_k}\left(\frac{\mu_t}{\sigma_k}\frac{\partial \overline{u_i' u_j'}}{\partial x_k}\right),$ where $\mu_t = \rho C_\mu \frac{k^2}{\varepsilon}$, $k = \frac{1}{2}\overline{u_i' u_i'}$, $C_\mu = 0.09$, and $\sigma_k = 0.82$	(T4)
- Molecular diffusion	$D_{L,ij} = \frac{\partial}{\partial x_k}\left[\mu \frac{\partial}{\partial x_k}\overline{u_i' u_j'}\right]$	(T5)
- Stress production	$P_{ij} = \rho\left(\overline{u_i' u_k'}\frac{\partial u_j}{\partial x_k} + \overline{u_j' u_k'}\frac{\partial u_i}{\partial x_k}\right)$	(T6)
- Pressure strain	$\varphi_{ij} = p'\left(\frac{\partial u_i'}{\partial x_j} + \frac{\partial u_j'}{\partial x_i}\right) \approx \varphi_{ij,1} + \varphi_{ij,2} + \varphi_{ij,w}$ [38], where $\varphi_{ij,1} \equiv -C_1 \rho \frac{\varepsilon}{k}\left[\overline{u_i' u_j'} - \frac{2}{3}\delta_{ij}k\right]$ with $C_1 = 1.8$, $\varphi_{ij,2} \equiv -C_2\left[\left(P_{ij} + \frac{5}{6}G_{ij} - C_{ij}\right) - \frac{2}{3}\delta_{ij}\left(P + \frac{5}{6}G - C\right)\right]$ with $C_2 = 0.60$, $P = 0.5 P_{kk}$, $G = 0.5 G_{kk}$, and $C = 0.5 C_{kk}$, $\varphi_{ij,w} \equiv C_1'\frac{\varepsilon}{k}\left(\overline{u_k' u_m'}n_k n_m \delta_{ij} - \frac{3}{2}\overline{u_i' u_k'}n_j n_k - \frac{3}{2}\overline{u_j' u_k'}n_i n_k\right)\frac{C_\ell k^{3/2}}{\varepsilon d} + C_2'\left(\varphi_{km,2}n_k n_m \delta_{ij} - \frac{3}{2}\varphi_{ik,2}n_j n_k - \frac{3}{2}\varphi_{jk,2}n_i n_k\right)\frac{C_\ell k^{3/2}}{\varepsilon d}$ with $C_1' = 0.5$, $C_2' = 0.3$, $C_\ell = C_\mu^{3/4}/\kappa$, $C_\mu = 0.09$, and $\kappa = 0.4187$	(T8)
- Dissipation tensor	$\varepsilon_{ij} = 2\mu \overline{\frac{\partial u_i'}{\partial x_k}\frac{\partial u_j'}{\partial x_k}} \approx \frac{2}{3}\delta_{ij}(\rho\varepsilon + 2\rho\varepsilon M_t^2)$ with $M_t = \sqrt{\frac{k}{a^2}}$,	(T9)
- Dissipation rate	$\frac{\partial}{\partial t}(\rho\varepsilon) + \frac{\partial}{\partial x_i}(\rho\varepsilon u_i) = \frac{\partial}{\partial x_j}\left[\left(\mu + \frac{\mu_t}{\sigma_\varepsilon}\right)\frac{\partial \varepsilon}{\partial x_j}\right]C_{\varepsilon1}\frac{1}{2}(P_{ii} + C_{\varepsilon3}P_{ii})\frac{\varepsilon}{k} - C_{\varepsilon2}\rho\frac{\varepsilon^2}{k},$ where $\sigma_\varepsilon = 1.0$, $C_{\varepsilon1} = 1.44$, $C_{\varepsilon2} = 1.92$, and $C_{\varepsilon3} = \tanh\left|\frac{u_\parallel}{u_\perp}\right|$	(T10)
- Turbulent kinetic energy at wall BC	$\frac{\partial}{\partial t}(\rho k) + \frac{\partial}{\partial x_i}(\rho k u_i) = \frac{\partial}{\partial x_j}\left[\left(\mu + \frac{\mu_t}{\sigma_{k1}}\right)\frac{\partial k}{\partial x_j}\right] + \frac{1}{2}(P_{ii} + G_{ii}) - \rho\varepsilon(1 + 2M_t^2)$ with $\sigma_{k1} = 1.0$	(T11)
- Standard wall functions	$\frac{\overline{u_\tau^2}}{k} = 1.098$, $\frac{\overline{u_\eta^2}}{k} = 0.247$, $\frac{\overline{u_\lambda^2}}{k} = 0.655$, $-\frac{\overline{u_\tau^2 u_\eta^2}}{k} = 0.255$	(T12)

Table 1. Continued

Name	Mathematical expression	Eq.
Discrete phase model (DPM)	$m_p = \dfrac{d\vec{u}_p}{dt} = m_P \dfrac{\vec{u} - \vec{u}_p}{\tau_r} + m_P \dfrac{\vec{g}(\rho_p - \rho)}{\rho_p}$, where $\tau_r = \dfrac{\rho_p d_p^2}{18\mu} \dfrac{24}{C_d Re}$ [37] and $Re \equiv \dfrac{\rho d_p |\vec{u}_p - \vec{u}|}{\mu}$	(T13)
- Particle turbulent dispersion	$D_P = \overline{u_i' u_j'} T_L$ with $T_L \approx C_L \dfrac{k}{\varepsilon}$ and $C_L = 0.3$ Velocity fluctuation: $u' = \zeta\sqrt{\overline{u'^2}}$, $v' = \zeta\sqrt{\overline{v'^2}}$, $w' = \zeta\sqrt{\overline{w'^2}}$ Eddy lifetime: $\tau_e = -T_L \ln(r)$, r is the uniform random number $\in [0,1]$ Particle eddy crossing time: $t_{cross} = \tau_r \ln\left[1 - \left(\dfrac{L_e}{\tau_r |u - u_p|}\right)\right]$	(T14)

approach [31,36], the gas flow is modeled as a continuous phase, described by the continuity in Eq. (T1) and momentum in Eq. (T2). Contrastingly, dispersed solid particles are treated as discrete phases, as expressed by the discrete phase model (DPM) in Eq. (T12). A two-way coupling method was used, which accounts for the interaction between the particles and fluid. The CFD model is coupled with the steady-state e-based RSM for turbulence in Eq. (T3), including the turbulent diffusion in Eq. (T4), molecular diffusion in Eq. (T5), stress production by rotation in Eq. (T6), linear pressure strain in Eq. (T7), dissipation tensor in Eq. (T8), scalar dissipation rate in Eq. (T9), and turbulent kinetic energy as the boundary condition (BC) in Eq. (T10).

In Table 1, $\overline{u}_i$ is the mean velocity, $\overline{P}$ is the mean pressure, ρ is the gas density, μ is the gas kinematic viscosity, u_i' is the fluctuation velocity of the ith component, and $\overline{u_i' u_j'}$ is the Reynolds stress tensor in Eq. (T3). In Eq. (T4), μ_t is the turbulent kinetic viscosity. In Eq. (7), the pressure strain term (φ_{ij}) is decomposed into slow $(\varphi_{ij,1})$, rapid $(\varphi_{ij,2})$, and wall reflection $(\varphi_{ij,w})$ terms. The $\varphi_{ij,w}$ is responsible for the redistribution of normal stresses near the wall, which tends to dampen the normal stress perpendicular to the wall while enhancing the stresses parallel to the wall. The dissipation rate tensor (ε_{ij}) in Eq. (T8) was modeled using the scalar dissipation rate (ε) in Eq. (T9) obtained from the standard $k-\varepsilon$ turbulence model. In Eq. (T8), $a(\equiv \sqrt{\gamma RT})$ is the speed of sound. In Eq. (T9), the $C_{\varepsilon3}$ factor was calculated from the correlation of the component of the flow velocity parallel to the gravitational vector $(u_\parallel)$ and the component of the flow velocity perpendicular to the gravitational vector $(u_\perp)$.

Except for the wall boundary conditions in Eq. (T10), the far-field turbulence kinetic energy (k) required for several terms, such as μ_t in Eq. (T4), $\varphi_{ij,1}$ and $\varphi_{ij,w}$ in Eq. (T7), M_t in Eq. (T8), and ε in Eq. (T9), was obtained directly from the Reynolds stress tensor $\left(k = \dfrac{1}{2}\overline{u_i' u_i'}\right)$. For the wall boundary conditions, k was estimated using the additional $k-\varepsilon$ transport equation in Eq. (T10). The other near-wall values of the Reynolds stresses were computed using Eq. (T11). In Eq. (T12), m_p is the particle mass, $\vec{u}_p$ is the fluid velocity, $\vec{u}_p$ is the particle velocity, ρ_p is the particle density, $m_p \dfrac{\vec{u} - \vec{u}_p}{\tau_r}$ is the drag force,

τ_r is the particle relaxation time [37], and Re is the relative Reynolds number.

The turbulent dispersion of the particles was modeled using the discrete random walk model [37,39] as a stochastic tracking method in Eq. (T13), where the particle diffusivity (D_p) was calculated using $\overline{u_i' u_j'}$ and Lagrangian integral time (T_L). The Gaussian-distributed random velocity fluctuation (u', v', and w') was defined with a normally distributed random number (ζ). The characteristic lifetime of the eddy (τ_e) was defined as a function of T_L and a uniform random number (r) between 0 and 1. The particle eddy crossing time (t_{cross}) was given by the particle relaxation time (τ_r), eddy length scale (L_e), and relative velocity magnitude ($|u-u_p|$). The particle is assumed to interact with the gas-phase eddy over the smaller of τ_e and t_{cross}. When this time was reached, new values of u', v', and w' were obtained by applying a new value of ζ.

In the two-way coupling method, five calculation steps were implemented: (i) solving the gas flow field, (ii) introducing the discrete phase, (iii) recalculating the fluid phase using an interphase exchange of momentum and mass during the previous particle calculation, (iv) recalculating the discrete phase trajectories in the modified gas flow field, and (v) repeating steps (iii) and (iv) until a converged solution is achieved. A maximum number of 500,000 steps and a step length factor of five were used to minimize the incomplete particles to less than 1% of the total particles tracked and track the particle trajectories.

2. Cyclone Geometry

Before examining the effect of the domed-roof cyclone on separation efficiency, a standard cyclone with a flat-roof, Stairmand high-efficiency cyclone [29] with a barrel diameter (D) of 0.29 m and a vortex finder diameter (D_e) of 0.5D was considered for comparison. The domed-roof cyclone geometry (D=0.29 m, D_e=0.5D) was created based on the Stairmand cyclone and the ASME mechanical strength requirement for internal pressure vessels [40]. The inlet duct elevation was reduced by D/12 from the domed-roof cyclone, respecting the ASME rule for an acceptable local thin area [40]. Because the vortex finder strongly affects the separation efficiency and pressure drop of cyclones [2,17,18,29,32,36], three diameters of the vortex finder were investigated with D_e=0.5D, 0.4D, and 0.3D. Fig. 2 shows the geometry of the four cyclone separators: (i) flat-roof cyclone with a vortex finder of 0.5D (F-0.5D), (ii) domed-roof
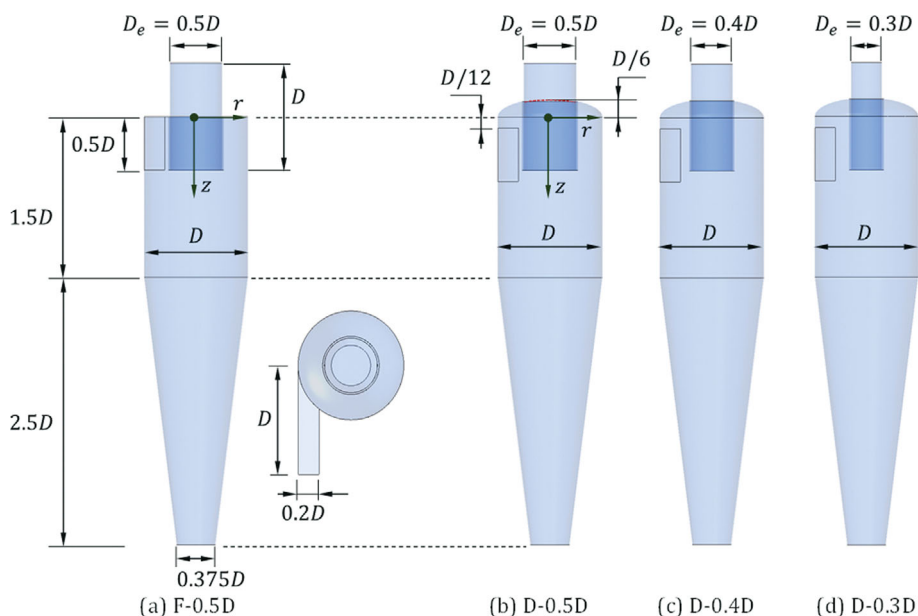
Fig. 2. Geometries for flat- (F-0.5D) and domed-roof (D-0.5D, D-0.4D, and D-0.3D) cyclones.

Table 2. Physical properties of gas and particles and boundary conditions for 13 cases

	Parameters	Air-CaCO₃ system				C₃H₆/H₂ - Polypropylene system							
Physical properties	ρ (kg/m³)	1.185 (air) [29]				23.45 [41]							
	μ (kg/m·s)	1.85×10⁻⁵ (air) [29]				1.14×10⁻⁵ [41]							
	ρ_p (kg/m³)	2740 [29], 2730 [1]				910 [41]							
	d_p (μm)	0.1-100 [29], 0.2-6.5 [1]				1-40 [7]							
Case		C1	C2	C3	C4	C5	C6	C7	C8	C9	C10	C11	C12	C13
Geometry name		F-0.5D		D-0.5D		D-0.5D			D-0.4D			D-0.3D		
Boundary conditions	P_{out} (bar)	1	1	1	1	20								
	u_{in} (m/s)	16.1	20	16.1	20	3	4	5	3	4	5	3	4	5
	m_s (kg/h)	1.62	2.01	1.62	2.01	0.07	0.09	0.12	0.07	0.09	0.12	0.07	0.09	0.12

cyclone with a vortex finder of 0.5D (D-0.5D), (iii) domed-roof cyclone with a vortex finder of 0.4D (D-0.4D), and (iv) domed-roof cyclone with a vortex finder of 0.3D (D-0.3D). The cone tip diameter (0.375D) was the same for all four cyclones. z and r are the axial and radial directions of the cyclone, respectively.

Table 2 reports the physical properties of gas and solid particles for two systems (air-CaCO₃ [1,29] and C₃H₆/H₂-Polypropylene [7, 41]) and boundary conditions for 13 cases (C1-C13) simulated in this study. The physical properties of the C₃H₆/H₂-PP system (Case number from C5 to C13) were obtained at 20 bar and 80 °C. C1 and C3 are used for the CFD model validation against experimental data [1,29]. C2 and C4 are performed using the same material properties and boundary conditions to identify the influence of the roof types (flat and domed) on separation performance. Keeping a constant solid to gas mass ratio of 2.8×10⁻³ kg_solid/kg_gas [29] (or inlet solid load of 3.32 g/m³), the particle feed rate (m_s, kg/h) was determined according to the inlet velocity (u_in) in C1-C4. The inlet particle size (d_p) of CaCO₃ was distributed from 0.1 to 100 μm [29], as shown in Fig. 3.

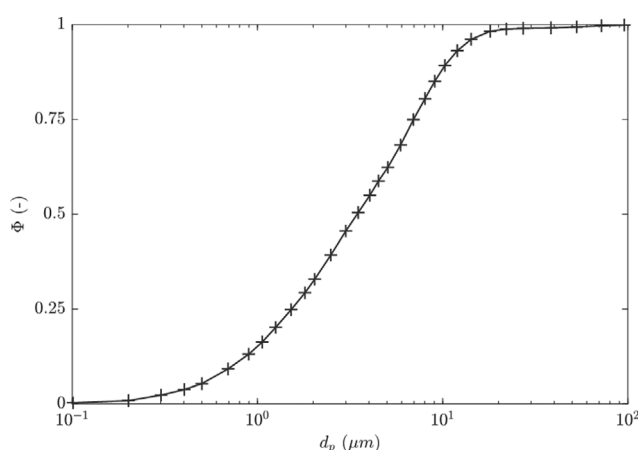The effects of the vortex finder diameter (0.5D, 0.4D, and 0.3D)

Fig. 3. Particle size distribution from 0.1 to 100 μm in the air-CaCO₃ system [29].

and inlet velocity (u_in=3, 4, and 5 m/s) on separation performance were investigated for C5-C13. m_s was calculated from a solid load

$D_e = 0.5D$

Front view

Top view

(a) F-0.5D

$D_e = 0.5D$

$D_e = 0.4D$

$D_e = 0.3D$

Front view   Top view
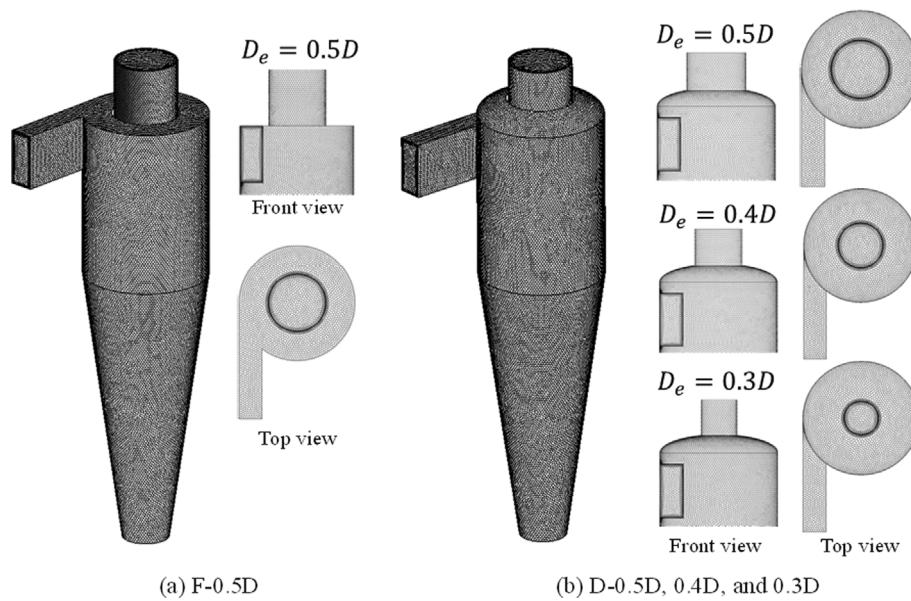
(b) D-0.5D, 0.4D, and 0.3D

Fig. 4. Three-dimensional (3D) mesh structures of the computational domain for flat- and domed-roof cyclones.

of 0.7619 g/m³ [7] for C5-C13. In the C_3H_6/H_2-PP system, the gas phase had a relatively high density, and the density of the solid particles was lower than that of $CaCO_3$ in C1-C4.

In CFD with the DPM model, a total of 1024 parcels, which is the same as the number of cells on the inlet surface of the cyclones, were injected uniformly through the inlet surface. The number of real particles in each parcel depended on the mass flow rate of each particle size, even though the number of parcels was identical for all 13 cases. For the simulation of grade separation tests in C1 and C3, 15 particle sizes from 0.2 to 6.5 μm in the same interval were applied to the boundary condition of CFD. For the grade separation tests in C5-C13, 20 particle sizes ranging from 1 to 40 μm were used for the boundary conditions.

3. Meshing Structure

The computational domain was discretized into polyhedral cells with thin near-wall inflation layers constructed using prism cells to capture the velocity gradients. The height of the first cell adjacent to the wall was estimated based on the y^+ criterion [42]:

$$y^+ = \frac{\rho y_p u_\tau}{\mu} \tag{1}$$

where $u_\tau = (\tau_w/\rho)^{0.5}$ is the friction velocity, y_p is the distance from the wall to the wall-adjacent cell center, ρ is the fluid density, and μ is the fluid viscosity. The wall shear stress (τ_w) is given by:

$$\tau_w = c_f(\rho u^2/2) \text{ with } c_f = (2\log(Re) - 6.5)^{-2.3} \text{ and } Re = \rho uL/\mu \tag{2}$$

where c_f is the skin friction coefficient, and u is the average velocity. The fluid Reynolds number (Re) was defined at the inlet face of the cyclone. The hydraulic diameter (L) of the inlet face is defined as

$$L = \sqrt{(4/\pi) \times 0.5D \times 0.2D}. \tag{3}$$

A value of $y^+ = 50$ near the initial location of the log-law layer was selected to estimate the wall-adjacent cell height for all the geome-

tries.

The minimum fluid boundary thickness (δ_{99}) was defined as follows to evaluate the suitable number of inflation layers [43]

$$\delta_{99} = \frac{0.38L}{Re^{0.2}} \text{ if } Re < 10^5; \; \delta_{99} = \frac{4.91L}{Re^{0.5}} \text{ if } Re \geq 10^5. \tag{4}$$

Because the first inflation layer height was estimated from y^+ and the total layer height was also controlled by δ_{99}, the number of inflation layers and layer size growth rate were chosen as 7 and 1.3, respectively, to match the cell size of the final inflation layer with that of the cyclone center.

Three mesh densities (coarse, medium, and fine) of the flat-roof cyclone in Fig. 4(a) were generated for the mesh independence test, targeting a minimum orthogonal quality higher than 0.3 and a cell maximum aspect ratio lower than 50. The mesh structures of the flat and domed cyclones on the medium mesh are shown in Fig. 4. For the flat-roof cyclone (F-0.5D), the number of cells (N_{cell}) on the coarse, medium, and fine meshes was 359355, 668288, and 1029827, respectively. The average grid sizes (δx) on the coarse, medium, and fine meshes were 5.4 mm, 4.4 mm, and 3.8 mm, respectively. For the three domed-roof cyclones in Fig. 4(b), N_{cell} is 674054, 658365, and 648690, respectively, having a mesh density ($\delta x = 4.4$ mm) similar to that of the medium mesh of F-0.5D.

4. Simulation Setup

The CFD simulation was executed on a workstation with 48 cores of an Intel Xeon CPU with 3.0 GHz and 256 GB RAM using a finite volume-based solver (ANSYS Fluent 2022 R2, ANSYS Inc., USA, 2022). Fixed velocities were set for the inlet boundary conditions, and particles were injected through the inlet area of the cyclones. The solid outlet boundary condition (cone tip) was set as the wall with a particle trap. The gas outlet boundary condition (top of the vortex finder) was set as the pressure outlet with particle escape.

The semi-implicit method for the pressure-linked equations

(SIMPLE) scheme was used to solve the Navier-Stokes equations. The pressure staggering option (PRESTO!) discretization scheme was used for pressure. The quadratic upstream interpolation for the convective kinematics (QUICK) scheme was selected for momentum discretization. The second-order upwind scheme was used to discretize the turbulent kinetic energy (k), turbulent dissipation rate (ε), and Reynolds stresses ($\overline{u_i'u_j'}$). The under-relaxation factors for the pressure, density, body forces, momentum, turbulent kinetic energy, turbulent dissipation rate, turbulent viscosity, Reynolds stresses, and discrete phase sources were set to 0.7, 1, 1, 0.7, 0.8, 0.8, 1, 0.5, and 0.5, respectively. A residual error of 1×10^{-5} was applied for convergence. A time step size of 0.0001 s was used for unsteady-state simulation, which was stopped when a stable state was reached for the pressure drop and volume-averaged axial velocity [44]. The steady-state simulation reached a stable state after around 12,000 iterations.

RESULTS AND DISCUSSION

A suitable mesh density for the CFD domain was first verified using the grid convergence index (GCI) method, focusing on key variables such as the Euler number ($Eu = \dfrac{\Delta P}{\frac{1}{2}\rho v_{in}^2}$) and cutoff diameter ($X_{50}$, or 50% separation efficiency) [12]. Subsequently, the CFD model for the flat-roof cyclone (F-0.5D) was validated against experimental data obtained from the literature [1,29]. It was confirmed that numerical results of steady-state simulation were in line with those of unsteady-state simulation for C1 (u_{in}=16.1 m/s). The flat-roof cyclone was compared with the domed-roof cyclone in terms of pressure drop (ΔP) and separation efficiency (η). Finally, an optimum diameter of the vortex finder was proposed for a domed-roof cyclone.

Fig. 5 presents the area-weighted average static pressure on the inlet surface and near-wall cells adjacent to the outlet surface in unsteady-state simulation. The pressure sampling interval was 0.01 s. The static pressure on the inlet surface was relatively stable, while that on the outlet surface was not stable because of swirling flows. Hoffman et al. [45] observed that the static pressure at an outlet near the wall was close to the outlet static pressure. Therefore, the static pressure near the outlet wall was selected for the comparison of outlet pressure between steady- and unsteady-state simulation. The two static pressures reached a converged value after around 0.7 s of the flow time (t). The steady-state pressure (dashed line in red) on the inlet surface was almost the same as that of unsteady state at t=0.7-1.0 s. There is a discrepancy between the pressure at the outlet wall (dashed line) in steady-state simulation and that (solid line) in unsteady-state simulation by 66 Pa, as shown in Fig. 5(b).

1. Mesh Independence Test Using Grid Convergence Index (GCI)

The grid resolution should be optimized to satisfy both numerical accuracy and computational cost [11,14,46]. Elsayed and Lacor [12] applied the GCI method suggested by Roache [46] to determine an asymptotic solution of grid convergence for cyclone CFD models. An extrapolation of the physical quantity obtained from the CFD simulation was estimated at a zero grid ($\delta x \rightarrow 0$, or an infinite number of cells). The GCI method quantitatively measures the extent to which the CFD results of a current grid size vary from those of the zero-grid one. The asymptotic solution was represented by an α factor [12] that was as close to one as possible. The detailed calculation steps for α are reported elsewhere [6,14,19,46]. Although the α value is sensitive to several factors, such as the investigated hydrodynamic parameters, grid size, geometry, and discretization method, a typical range of $0.95 \leq \alpha \leq 1.05$ is acceptable for determining an optimum mesh structure [6,14].

Fig. 6 illustrates the Eu and X_{50} values with respect to the values obtained from the coarse, medium, and fine meshes and zero-grid extrapolation ($\delta x \rightarrow 0$). For the F-0.5D cyclone, the deviation
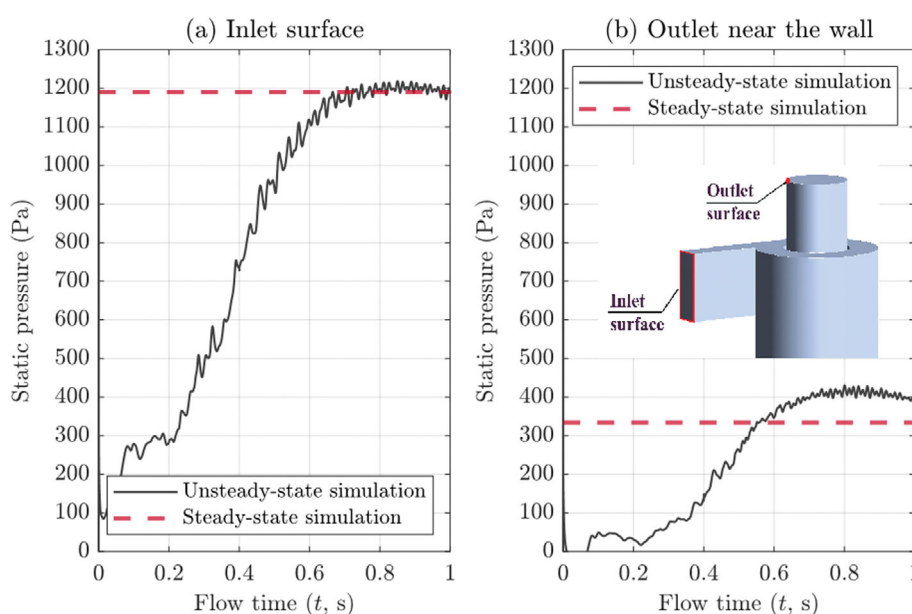

Fig. 5. Area-weighted average static pressure on the inlet surface and near-wall cells adjacent to the outlet surface.
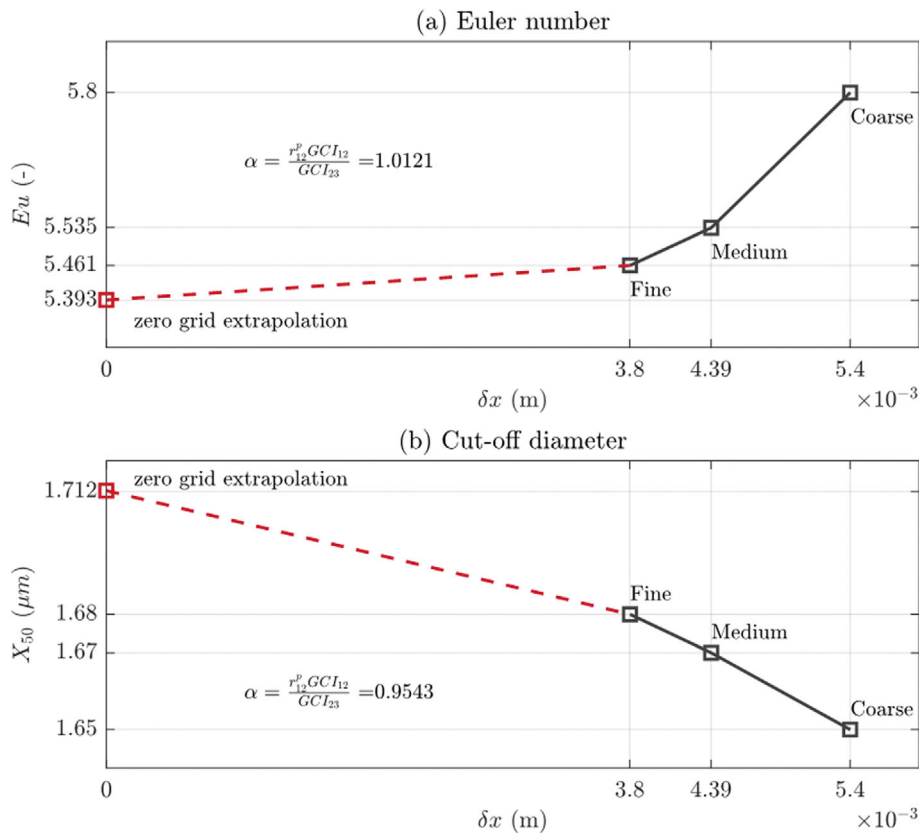
Fig. 6. Mesh independence test with respect to Euler number (Eu) and cut-off diameter (X$_{50}$) using the grid convergence index (GCI) method.

between δx=4.39 mm (medium) and $\delta x \rightarrow$0 mm for Eu and X$_{50}$ is 2.6% and 2.5%, respectively. The α values for Eu and X$_{50}$ are 1.0121 and 0.9543. Because the α values for both Eu and X$_{50}$ are in the range of 0.95 to 1.05, the medium mesh was chosen as an acceptable mesh density capable of obtaining asymptotic solutions. It is expected that the mesh density (δx=4.39) is applicable to domed-roof cyclones with a geometry similar to that of flat-roof cyclones.

2. CFD Model Validation
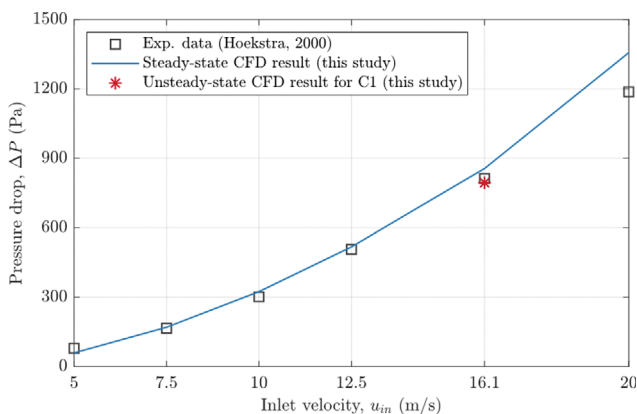
Fig. 7 shows the CFD results of the pressure drop (ΔP) of F-0.5D

Fig. 7. Validation of pressure drop (ΔP) with respect to the inlet velocity (u$_{in}$) against experimental data obtained from Hoeksta [29].

with respect to the inlet velocity (u$_{in}$) compared to the experimental data obtained from Hoekstra [29]. The ΔP agrees well with the experimental points for the range u$_{in}$=5-20 m/s. The pressure drop (ΔP) obtained from steady-state and unsteady-state simulations of C1 (flat-roof cyclone at u$_{in}$=16.1 m/s) was 856 and 794 Pa, respectively, and showed a difference of 7.2%.

The largest difference (170 Pa) between the CFD results and experimental data appeared at 20 m/s, showing a 14.3% deviation from the experimental point. The root mean square error (RMSE) between the CFD and experimental data was calculated as follows:

$$\text{RSME} = \sqrt{\frac{\sum_{i=1}^{n_p}(\phi_{CFD} - \phi_{exp})^2}{n_P}}, \tag{5}$$

where ϕ is the quantity, and n$_p$ is the number of data points. The RMSE of ΔP was 74 Pa, approximately 13% of the deviation from the experimental data.

Fig. 8 compares steady- and unsteady-state CFD results for the normalized tangential (u$_t$/u$_{in}$) and axial (u$_a$/u$_{in}$) velocities at z/D= 0.75 against experimental measurements [29] in the F-0.5D cyclone for u$_{in}$=16.1 m/s (C1 in Table 2). Here, r/R=0 indicates the transversal center of the cyclone body, while r/R=±1 represents the two wall sides of the cyclone body. The CFD results reasonably captured the experimental profiles of u$_t$ and u$_a$ in the radial direction (r). For steady state simulation, the RMSEs of u$_t$/u$_{in}$ and u$_a$/u$_{in}$ against the 42 experimental data are 0.2371 and 0.1216, respectively. For unsteady state simulation, those RMSEs are 0.2783 and 0.0958,
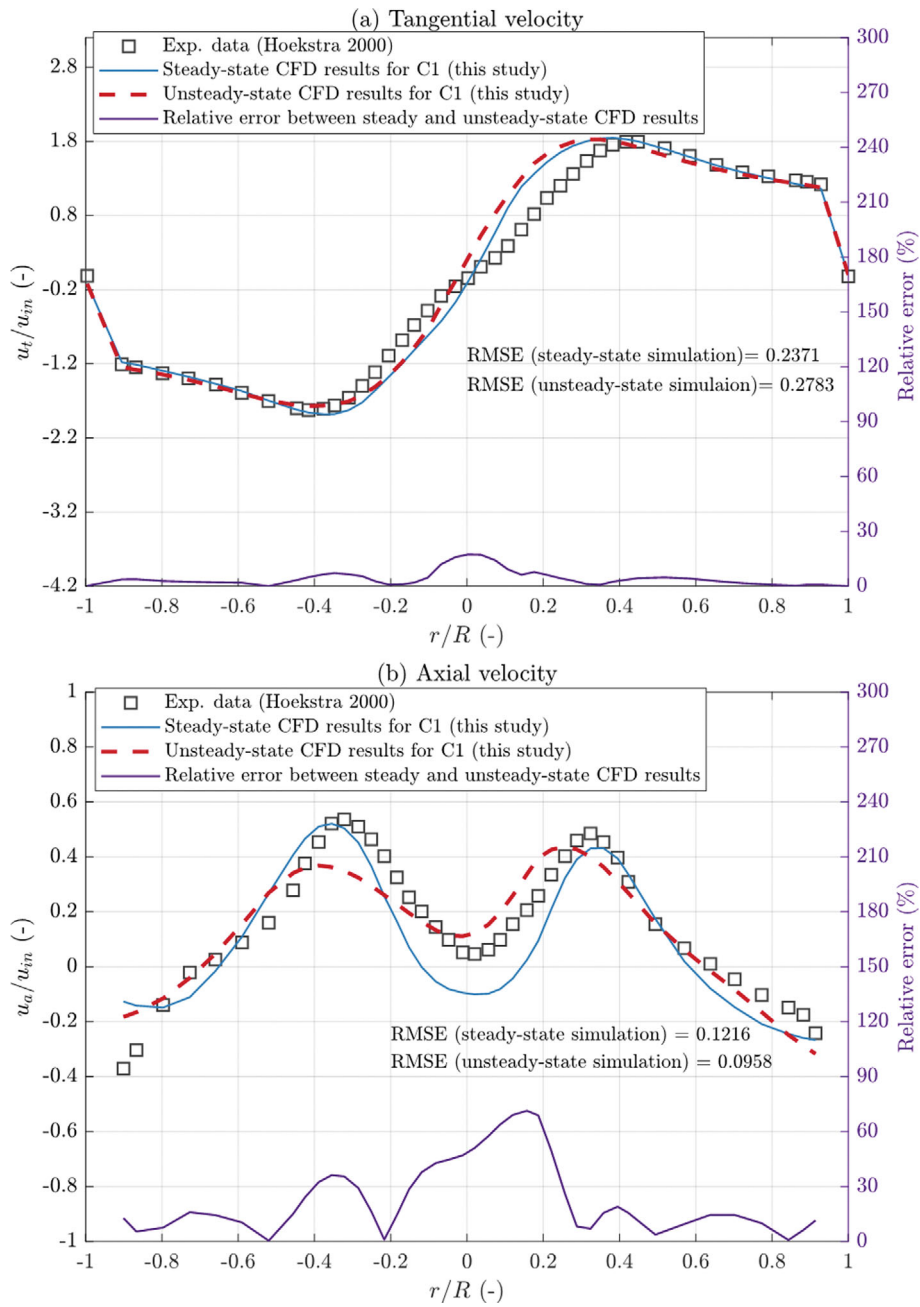
Fig. 8. Comparisons of dimensionless tangential (u_t/u_{in}) and axial (u_a/u_{in}) velocities of steady- and unsteady-state CFD results with experimental data [29] at z/D=0.75.

respectively. The large deviations of u_t and u_a between CFD and experimental data are found around $-0.3 \leq r/R \leq 0.3$ because of the strong swirling flows at the center of the cyclone [6]. The right y-axis in Fig. 8 indicates the relative error $\left| RE\ (\%) = 100 \times \left| \dfrac{u^{steady} - u^{unsteady}}{u_{max}^{unsteady}} \right| \right|$ between the steady and unsteady-state CFD results of u_t and u_a. The RE of u_t is higher than that of u_a, where the variation amplitude of u_t is wider than the that of u_a. The REs are bigger at the center than at the walls due to the strong swirling flows. The mean relative errors (MREs) of u_t and u_a are 4.6% and 25.4%, respectively. Although the

MRE of u_a/u_{in} is high, the absolute values of u_a/u_{in} are relatively small compared to those of u_t/u_{in}. Since the deviations between steady- and unsteady-state simulations in terms of ΔP, u_t, and u_a were not significant, steady-state simulation was used for further investigation to save computational time.

3. Hydrodynamics of Flat and Domed-roof Cyclones at Ambient Pressure

This study focused on the influence of the cyclone geometry (flat-roof and domed-roof) on the separation efficiency rather than the influence of operation conditions at high and low pressures. Hydrodynamics, such as pressure (P), tangential (u_t), and axial (u_a) veloc-
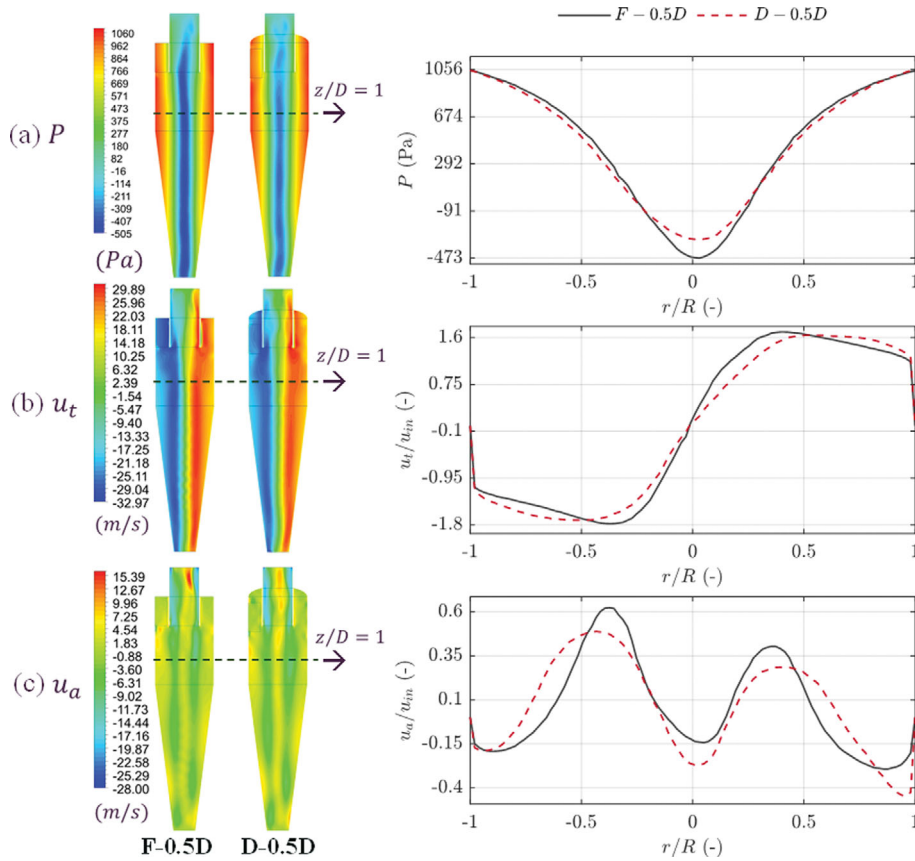
Fig. 9. Contours of pressure (P), tangential (u_t), and axial (u_a) velocities, and radial profiles of pressure (P), normalized tangential velocity (u_t/u_{in}), and normalized axial velocity (u_a/u_{in}) at z/D=1 for C1 (F-0.5D, u_{in}=16.1 m/s) and C3 (D-0.5D, u_{in}=16.1 m/s).

ity, was compared for the flat- and domed-roof cyclones, C1 and C3 (see Table 2), respectively, to identify the flow characteristics of the two cyclones at ambient pressure. Fig. 9 shows the contours of P, u_t, u_a, and the radial profiles of P, u_t/u_{in}, and u_a/u_{in}, at z/D=1. The pressure discrepancy between the center (r/R=0) and wall (r/R= ±1) sides of F-0.5D was 147 Pa higher than that of D-0.5D. Although the wall-adjacent pressures of the two cases were similar, the central pressure of F-0.5D decreased more than that of D-0.5D. This may be attributed to the fact that geometrical differences, such as a slightly longer cyclone barrel with a domed-roof, loosen the swirling flows and lead to a lower pressure drop at the center (see Fig. 9(a)).

The difference between the maximum and minimum values of u_t/u_{in} for D-0.5D (C3) is lower than the difference for F-0.5D (C1) in the center region ($-0.5 \leq r/R \leq 0.5$), as shown in Fig. 9(b). This resulted in a weak swirling flow in the central region for D-0.5D (C3). However, as shown in Fig. 9(c), the axial velocity of D-0.5D in the gravity direction at the center (r/R=0) is stronger than that of F-0.5D, whereas the upward velocity of D-0.5D is weaker than that of F-0.5D. Because the fine particles congregate around the center [47], the strong downward flow at the center helps capture the fine particles.

A comparison between the experimental measurements of Zhao [48], Hoffmann and Stein [1], and CFD results for the fractional separation efficiency (η_{frac}) for particle sizes ranging from 0.01 μm

to 10 μm is shown in Fig. 10. The total separation efficiency (η_{tot}) of the CFD was obtained from η_{frac} as follows:

$$\eta_{tot} = \Sigma_i^{N_p} \eta_{frac, i} x_i, \tag{6}$$

$$\eta_{frac} = \frac{N_i^{collect}}{N_i^{injected}}, \tag{7}$$

where N_p is the number of mass fractions for all particle sizes, and x_i is the mass fraction of an ith particle size ($\Sigma_i^{N_p} x_i = 1$). $N_i^{injected}$ and $N_i^{collect}$ are the number of ith particle sizes at the inlet and collecting outlet, respectively. One particle size was injected, and the collected particles were measured in the grade separation test to obtain η_{frac}. A total of 86 particle sizes were used by Hoffmann and Stein [1]. Twenty particle sizes were tested in the CFD simulations for F-0.5D (C2) and D-0.5D (C4). The diameters (D) of the cyclone barrels were different for the two experiments and the CFD simulations. However, the gas and particle properties, solids loadings, and geometric ratios of the cyclones were the same.

Zhao [48] performed an inlet velocity (u_{in}=20.18 m/s) in a F-0.5D cyclone with D=0.3 m [48]. Hoffmann and Stein [1] evaluated the separation efficiency using an F-0.5D cyclone with D=0.2 m and an inlet velocity u_{in}=15 m/s [1]. As shown in Fig. 10, η_{frac} of C2 (F-0.5D) and C4 (D-0.5D) agreed well with the experimental data of Zhao [48], except for d_p less than 1 μm. For $d_p \geq 1$ μm, η_{frac} of C2 was slightly higher than that of C4. The maximum value of η_{frac} (100%)
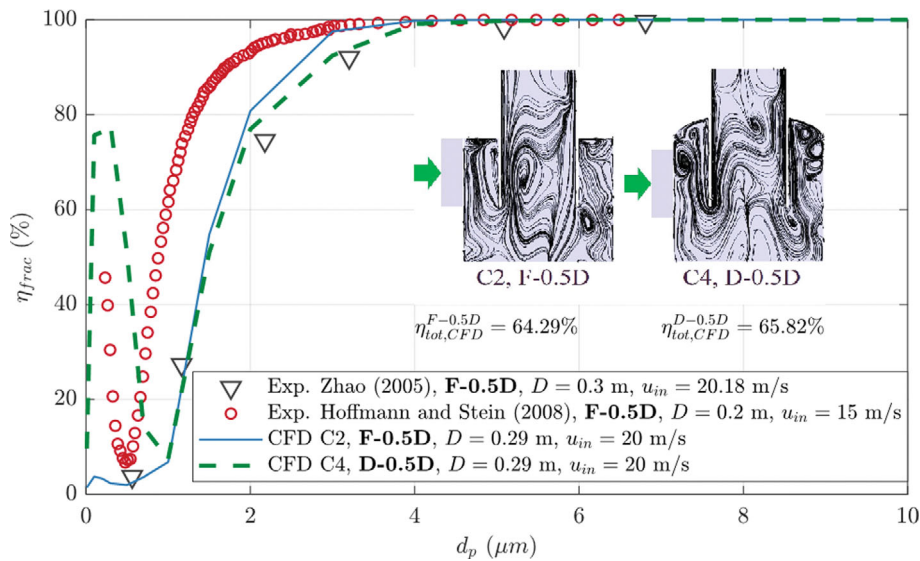
Fig. 10. Grade separation efficiency for C2 (F-0.5D, u_{in}=20 m/s) and C4 (D-0.5D, u_{in}=20 m/s) compared with experimental data [1,48].
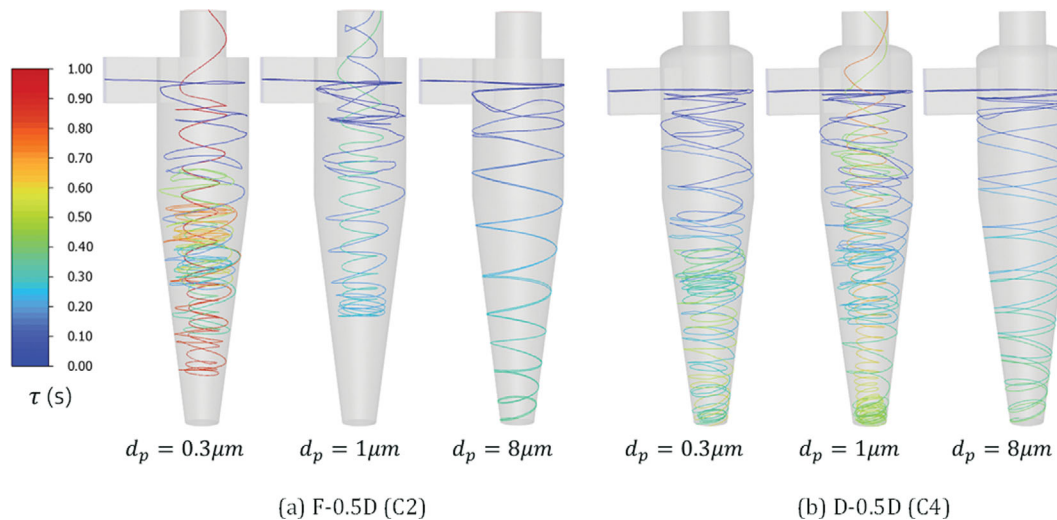

Fig. 11. Tracking trajectory of a particle with d_p=0.3, 1, and 8 μm for C2 (F-0.5D, u_{in}=20 m/s) and C4 (D-0.5D, u_{in}=20 m/s).

for both C2 and C4 was achieved for $d_p \geq 6$ μm. For fine particles ($d_p < 1$ μm), a tail where η_{frac} increases with decreasing d_p was observed by Hoffmann and Stein [1] and the domed-roof cyclone (D-0.5D). The domed-roof cyclone (D-0.5D) captured more solid particles of less than 1 μm than the flat-roof cyclone (F-0.5D) due to the stronger downward velocity (see Fig. 9(c)); the total separation efficiency of D-0.5D ($\eta_{tot, CFD}^{D-0.5D}$) was higher than that of F-0.5D ($\eta_{tot, CFD}^{F-0.5D}$).

The tails of high η_{frac} obtained from Hoffmann and Stein [1] and domed-roof cyclone CFD (C4) for $0 < d_p < 1$ μm were known as a fish-hook effect caused by recirculation eddies [49,50]. Since the recirculation eddies are promoted at the top side of the domed-roof cyclone (see two insets in Fig. 10), the entrained fine particles stay at the top side, which reduces fine particles escaping the cyclone.

The peak for η_{frac} of C4 in the tail was 78% at d_p=0.3 μm, whereas the peak of C2 in the tail was only 4% at d_p=0.1 μm. Fig. 11 shows the tracking history of the three particle sizes (0.3, 1, and 8 μm) for

C2 (F-0.5D) and C4 (D-0.5D). The color of the trajectory represents the residence time of the particles (τ, s). For d_p=0.3 μm, the residence time of C2 is longer, and the trajectory length is shorter than that of C4. It implies that η_{frac} of C4 (domed-roof cyclone) at d_p= 0.3 μm is higher than that of C2, as shown in Fig. 10. For d_p=1 μm, some particles escaped the cyclones for C2 and C4. The trajectory length of C4 was longer than that of C2, and η_{frac} of C4 was slightly higher than that of C2 (see Fig. 10). For d_p=8 μm, the residence time of C2 was shorter, and the trajectory line was simpler than that of C4. The η_{frac} of C2 is higher than that of C4. Most of the particles for d_p=8 μm are trapped, and η_{frac} of both C2 and C4 is close to 100% (see Fig. 10).

4. Hydrodynamics of Domed-roof Cyclones in High-pressure Polypropylene Production Process

As mentioned, cyclone performance depends on the geometry, inlet gas velocity, and particle properties. The effects of the vortex
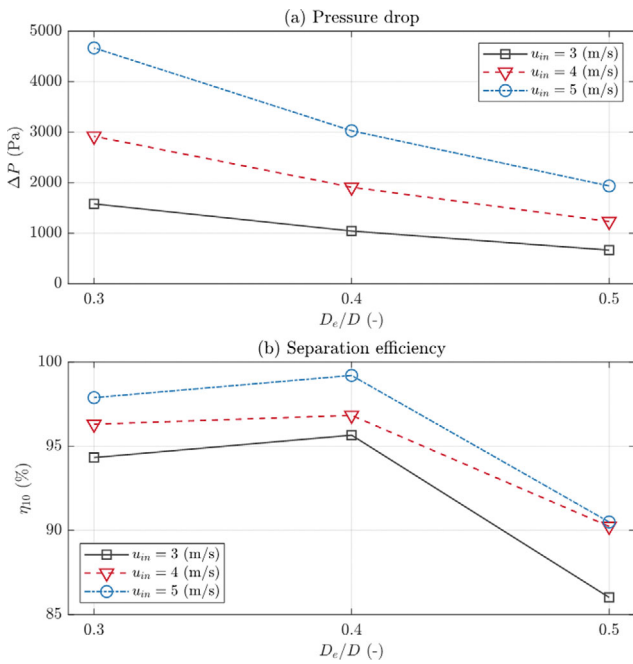
Fig. 12. Performance evaluation of domed-roof cyclone for vortex finder sizes (D_e/D) and inlet velocities (u_{in}) at 20 bar and 80 °C for the PP production process (C5-C13).

finder's diameter (D_e/D) and inlet velocity (u_{in}) on the pressure drop (ΔP) and separation efficiency (η_{10}) of d_p=10 μm of PP were investigated for the domed-roof cyclone at 20 bar and 80 °C (C5-C13, see Table 2), as shown in Fig. 12. Although the domed-roof cyclones have the advantage of collecting fine particles, the vortex finder diameter (D_e) of a domed-roof cyclone must be adjusted to improve the separation efficiency satisfying allowable pressure drop. The D_e influences the diameter of the inner vortex core, vortex length, and pressure drop [1]. The ΔP is proportional to the outlet velocity of the vortex finder. A small D_e/D and a high u_{in} led to an increase in ΔP. The minimum value (664 Pa) of ΔP is found at D_e/D=0.5 and u_{in}=3 m/s, and the maximum value (4,669 Pa) is found at D_e/D= 0.3 and u_{in}=5 m/s (see Fig. 12(a)).

The maximum separation efficiency (η_{10}) appears at D_e/D=0.4 for every u_{in}, as shown in Fig. 12(b). As mentioned in Section 2, the minimum separation efficiency must exceed 90% for a wide range of u_{in}, and D-0.5D (D_e/D=0.5) is inappropriate for the separation of PP particles. A small vortex finder enhances the separation efficiency with a trade-off of ΔP. In this study, the D_e/D=0.4 was chosen as the best design to maximize η_{10} with a moderate ΔP.

In Fig. 13, P, u_t, and u_a are compared for the domed-roof cyclones with D_e=0.4D (C8-C10) to identify the flow characteristics of the three cyclones at three u_{in}. The contours of P, u_t, and u_a, as well as the radial profiles of P, u_t/u_{in}, and u_a/u_{in}, at z/D=1, are shown in
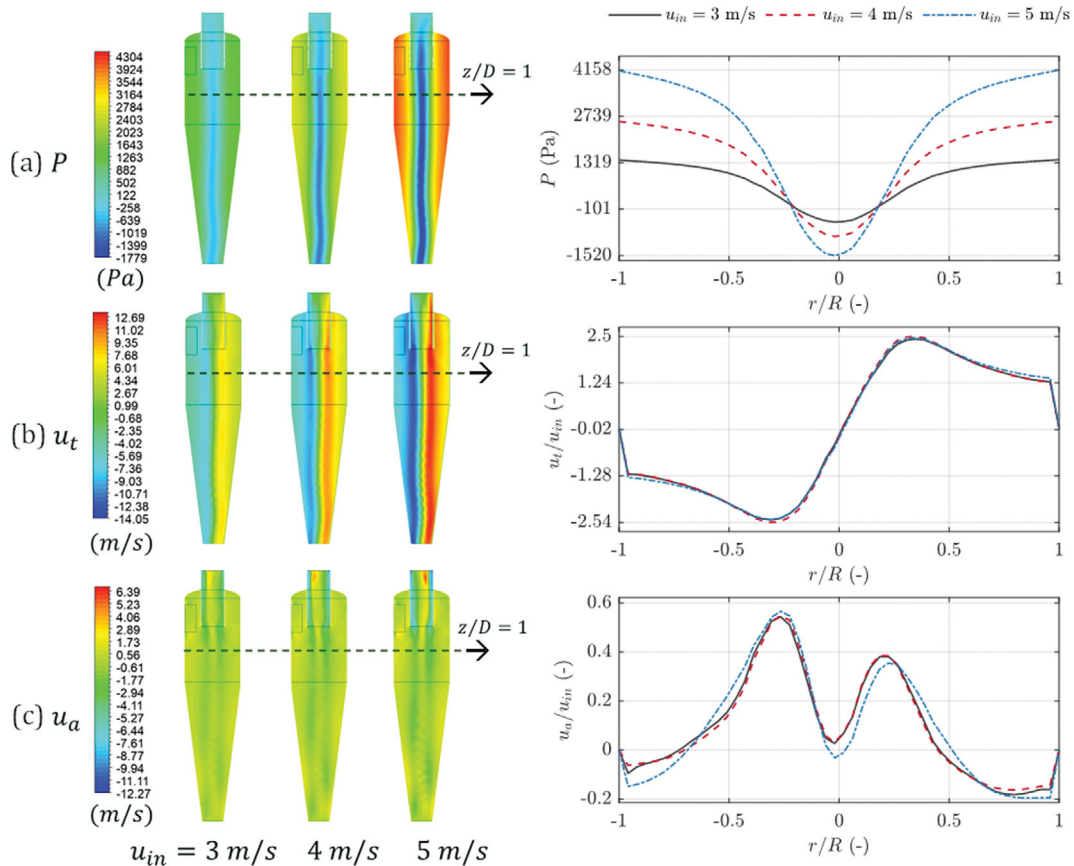

Fig. 13. Contours of pressure (P), tangential (u_t), and axial (u_a) velocities, and radial profiles of pressure (P), normalized tangential velocity (u_t/u_{in}), and normalized axial velocity (u_a/u_{in}) at z/D=1 for C8 (D-0.4D, u_{in}=3 m/s), C9 (D-0.4D, u_{in}=4 m/s), and C10 (D-0.4D, u_{in}= 5 m/s).

Table 3. Pressure drop (ΔP) and separation efficiency (η) of 13 cases

Geometry name	Air-CaCO₃*				C₃H₆/H₂ - Polypropylene**								
	F-0.5D		D-0.5D		D-0.5D			D-0.4D			D-0.3D		
Case	C1	C2	C3	C4	C5	C6	C7	C8	C9	C10	C11	C12	C13
u_{in} (m/s)	16.1	20	16.1	20	3	4	5	3	4	5	3	4	5
ΔP (Pa)	856	1357	793	1252	664	1233	1935	1043	1911	3029	1580	2920	4669
η (%)	62.1	64.3	62.9	65.8	86.0	90.2	90.5	95.7	96.8	99.2	94.3	96.3	97.9

* η is the total separation efficiency of the inlet particle data from [29].
** η is the grade separation efficiency for d_p=10 μm PP particles.

Fig. 13. The pressure discrepancy between the center (r/R=0) and wall (r/R=±1) sides of D-0.4D at u_{in}=5 m/s (C10) was the highest among the three D-0.4D cyclones (see Fig. 13(a)). The swirling flow of C10 is strongly developed owing to the high pressure difference, which leads to high separation efficiency.

The difference between the three u_t/u_{in} values of C8-C10 was not perceptible, as shown in Fig. 13(b). The axial velocity of C10 in the gravity direction at the center (r/R=0) was the lowest among the three cases (Fig. 13(c)). The strong downward flow of C10 at the center helped capture the fine particles, as mentioned previously.

Table 3 summarizes the performance of the 13 cases in terms of pressure drop (ΔP) and separation efficiency (η). The D-0.5D cyclones (C3 and C4) have a slight advantage in ΔP and η over the F-0.5D cyclones (C1 and C2) for the air-CaCO₃ system within the investigated range of u_{in}. At a velocity of 16.1 m/s, ΔP of the domed-roof cyclone (C3) is reduced by 65 Pa, and η increases by 0.8% compared to the flat-roof cyclone (C1). In the PP system (C5-C13), ΔP of the domed-roof cyclones is proportional to u_{in} and inversely proportional to D_e/D. The highest separation efficiency for d_p= 10 μm (η=99.2%) was achieved at u_{in}=5 m/s and D_e/D=0.4. For D_e/D=0.5 (C5-C7), the u_{in} should be higher than 4 m/s to sustain η≥90%. D_e/D=0.3 (C11-C13) is not recommended because of its high ΔP and low η.
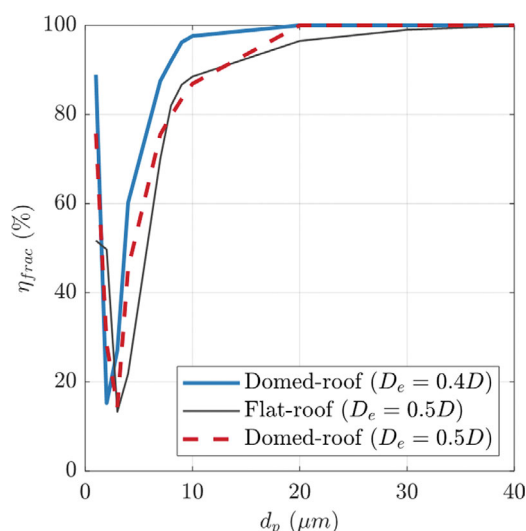

Fig. 14. Grade separation efficiency (η_{frac}) of F-0.5D, D-0.5D, and D-0.4D (C9) cyclones for the PP system at u_{in}=4 m/s, T=80°C, P_{out}=20 bar, and m_s=0.09 kg/h.

Fig. 14 highlights η_{frac} of the F-0.5D, D-0.5D (C6), and D-0.4D (C9) cyclones for the PP system at u_{in}=4 m/s, T=80°C, P_{out}=20 bar, and m_s=0.09 kg/h. The D-0.4D cyclone shows the best η_{frac} for d_p=1-40 μm among the three cyclones. The average η_{frac} of the D-0.4D cyclone is 8.4% higher than that of the F-0.5D cyclone. The ΔP of the D-0.4D cyclone (1,911 Pa, see Table 3) is 6.4% lower than that of the F-0.5D cyclone (2,034 Pa). As previously discussed, the fish-hook effect due to recirculation eddies produces a high η_{frac} for fine particles less than 5 μm. For the PP system, the fish hook effect can be reinforced by high gas density such as hydro-cyclones [51-53].

CONCLUSION

The separation performance of a high-pressure cyclone with a domed-roof was investigated for the polypropylene (PP) production process at 20 bar and 80°C using computational fluid dynamics (CFD). The Reynolds stress model (RSM) for gas turbulence and the two-way coupled discrete phase model (DPM) for solid particles were incorporated into the CFD model. The domed-roof cyclone was designed based on an industrial Stairmand high-efficiency cyclone and the mechanical strength requirements according to the ASME standard for high-pressure vessels. An appropriate mesh structure was selected using the grid convergence index (GCI) method. The CFD model was validated against experimental data of the pressure drop and tangential and axial velocities for a flat-roof cyclone in an air-CaCO₃ system at ambient pressure.

Because of the stable vortex length appearing at the longitudinal center of the cyclone, the separation efficiency (η) of the domed-roof cyclone was slightly higher than that of the flat-roof cyclone, particularly for fine particle sizes (d_p≤1 μm). The domed-roof cyclone at 20 bar and 80°C in the PP production process exhibited the best η and moderate ΔP when the vortex finder diameter was 40% of the diameter of the cyclone barrel. An increase in η was observed following an increase in the inlet velocity in the range of 3-5 m/s. The optimized domed-roof cyclone achieved an 8.4% higher mean fractional separation efficiency and a 6.4% lower pressure drop than a standard flat-roof cyclone for the PP production process at 20 bar and 80°C, with particle sizes ranging from 1 to 40 μm. This study demonstrated that a domed-roof cyclone outperformed a flat-roof cyclone for fine particles.

ACKNOWLEDGEMENTS

NOMENCLATURE

a　　　: speed of sound [m/s]
c_f　　: skin friction coefficient
d　　　: the normal distance to the wall [m]
d_p　　: particle diameter [m, μm]
D　　　: cyclone barrel diameter [m]
D_e　　: vortex finder diameter [m]
$D_{T,ij}$　: turbulence diffusion [m²/s]
$D_{L,ij}$　: molecular diffusion [m²/s]
D_P　　: particle diffusivity [m²/s]
Eu　　: Euler number
$\vec{g}$　　: gravity vector [9.81 m/s²]
k　　　: turbulence kinetic energy [m²/s²]
L　　　: hydraulic diameter [m]
L_e　　: eddy length scale [m]
m_p　　: particle mass [kg]
m_s　　: particle feed rate [kg/h]
n_P　　: number of points
n_{frac}　: fractional separation efficiency [%]
n_{tot}　: total separation efficiency [%]
N_p　　: number of particle sizes
N_{cell}　: number of cells
N_{mesh}　: total number of meshes
P　　　: pressure [Pa]
P_{out}　: pressure outlet [Pa]
$\overline{P}$　　: mean pressure [Pa]
P_{ij}　　: stress production term
ΔP　　: pressure drop [Pa]
r　　　: radial direction coordinate [m]
R　　　: cyclone radius [m]
Re　　: Reynolds number
t　　　: time [s]
Δt　　: pseudo time step for each cell in the domain [s]
T_L　　: Lagrangian integral time [s]
t_{cross}　: particle eddy crossing time [s]
$\vec{u}$　　: fluid velocity vector [m/s]
$\vec{u}_p$　　: particle velocity vector [m/s]
$\overline{u}_i$　　: mean velocity [m/s]
u_i'　　: fluctuation velocity of number i component [m/s]
$\overline{u_i'u_j'}$　: Reynolds stress tensor
u_a　　: axial velocity [m/s]
u_{in}　　: inlet velocity [m/s]
u_t　　: tangential velocity [m/s]
u_τ　　: friction velocity [m/s]
$u_∥$, $u_⊥$: gravitational vector
V　　　: volume of computational domain [m³]
X_{50}　: cut-off diameter [m, μm]
x_i　　: mass fraction of particle size
y^+　　: dimensionless wall distance
y_p　　: distance from the wall to the first cell [m]

z　　　: axial direction coordinate [m]

Greek Letters

α　　: asymptotic range of convergence solution
δ_{99}　: minimum fluid boundary thickness [m]
δ_x　: average grid size [m]
η　　: separation efficiency [%]
η_{10}　: fractional separation efficiency for d_p=10 μm [%]
ε　　: turbulence dissipation rate [m²/s³]
ε_{ij}　: dissipation rate tensor
ζ　　: Gaussian normally distributed random number
μ　　: gas kinematic viscosity [Pa·s]
μ_t　　: turbulent kinetic viscosity [Pa·s]
φ_{ij}　: pressure strain term
ϕ　　: physical quantities of data
ρ　　: density of gas [kg/m³]
ρ_p　　: density of particle [kg/m³]
τ　　: residence time [s]
τ_r　　: particle relaxation time [s]
τ_e　　: characteristic lifetime of the eddies [s]
τ_w　　: wall shear stress [Pa]

REFERENCES

1. A. C. Hoffmann and L. E. Stein, *Gas cyclones and swirl tubes: Principles, design and operation*, Springer, Berlin (2008).

2. Z. W. Zhang, Q. Li, Y. H. Zhang and H. L. Wang, *Sep. Purif. Technol.*, **286**, 120394 (2022).

3. J. Song, Y. Wei, G. Sun and J. Chen, *Chem. Eng. J.*, **309**, 249 (2017).

4. P. Khalili Ata Abadi, J. Vaziri Naeen Nejad and S. Kheradmand, *Chem. Eng. Res. Des.*, **179**, 331 (2022).

5. S. Jiang, H. Yuan, F. Zhou and S. Fu, *Chem. Eng. Process.*, **164**, 108398 (2021).

6. N. Fathizadeh, A. Mohebbi, S. Soltaninejad and M. Iranmanesh, *J. Nat. Gas Sci. Eng.*, **26**, 313 (2015).

7. A. Dumain and C. Raufast, US Patent, 4,882,400 (1989).

8. J. a. B. P. Soares and T. F. L. McKenna, *Polyolefin reaction engineering*, Wiley-VCH Verlag & Co. KGaA, Weinheim, Germany (2012).

9. A. Rita and O. D. Figueiredo, Master's Thesis, University of Lisbon, Lisbon (2015).

10. R. Fan, PhD Thesis, Iowa State University, Ames (2006).

11. S. I. Ngo and Y.-I. Lim, *ChemEngineering*, **4**, 23 (2020).

12. K. Elsayed and C. Lacor, *Comput. Fluids*, **51**, 48 (2011).

13. S. I. Ngo, Y.-I. Lim, B.-H. Song, U.-D. Lee, J.-W. Lee and J.-H. Song, *Powder Technol.*, **275**, 188 (2015).

14. S. I. Ngo, Y. I. Lim, D. Lee, M. W. Seo and S. Kim, *Energy Convers. Manage.*, **233**, 113863 (2021).

15. Y. Park, C. Y. Yun, J. Yi and H. Kim, *Korean J. Chem. Eng.*, **22**, 697 (2005).

16. E. Hosseini, H. Fatahian and E. Fatahian, *Korean J. Chem. Eng.*, **39**, 3482 (2022).

17. E. Yohana, M. Tauviqirrahman, D. A. Laksono, H. Charles, K.-H. Choi and M. E. Yulianto, *Powder Technol.*, **399**, 117235 (2022).

18. X. Wu and X. Chen, *Environ. Prog. Sustain. Energy*, **38**, 1 (2019).

19. K. Elsayed and C. Lacor, *Appl. Math. Model.*, **35**, 1952 (2011).

20. K. Jang, G. G. Lee and K. Y. Huh, *Comput. Fluids*, **172**, 274 (2018).

21. W. D. Griffiths and F. Boysan, *J. Aerosol Sci.*, **27**, 281 (1996).
22. S. Venkatesh, M. Sakthivel, M. Avinasilingam, S. Gopalsamy, E. Arulkumar and H. P. Devarajan, *Korean J. Chem. Eng.*, **36**, 929 (2019).
23. Y. Sun, J. Yu, W. Wang, S. Yang, X. Hu and J. Feng, *Korean J. Chem. Eng.*, **37**, 743 (2020).
24. Y. Xu, B. Tang, X. Song, Z. Sun and J. Yu, *Korean J. Chem. Eng.*, **35**, 2355 (2018).
25. R. Shastri and L. S. Brar, *Sep. Purif. Technol.*, **249**, 117149 (2020).
26. S. K. Shukla, P. Shukla and P. Ghosh, *Appl. Math. Model.*, **37**, 5774 (2013).
27. S. Pandey and L. S. Brar, *Powder Technol.*, **407**, 117629 (2022).
28. F. Kaya and I. Karagoz, *Chem. Eng. J.*, **151**, 39 (2009).
29. A. J. Hoekstra, PhD Thesis, Delft University of Technology, Delft (2000).
30. T. E. Nowlin and K. P. Wagner, US Patent, 4,481,301 (1984).
31. M. Wasilewski, *Sep. Purif. Technol.*, **179**, 236 (2017).
32. F. Parvaz, S. H. Hosseini, G. Ahmadi and K. Elsayed, *Sep. Purif. Technol.*, **187**, 1 (2017).
33. H. Safikhani, *Adv. Powder Technol.*, **27**, 2277 (2016).
34. A. Raoufi, M. Shams, M. Farzaneh and R. Ebrahimi, *Chem. Eng. Process.*, **47**, 128 (2008).
35. H. Safikhani, J. Zamani and M. Musa, *Adv. Powder Technol.*, **29**, 611 (2018).
36. K. Elsayed and C. Lacor, *Comput. Fluids*, **71**, 224 (2013).
37. A. D. Gosman and E. loannides, *J. Energy*, **7**, 482 (1983).
38. M. M. Gibson and B. E. Launder, *J. Fluid Mech.*, **86**, 491 (1978).
39. A. Fluent, ANSYS Fluent theory guide, ANSYS Inc. (2022).
40. ASME, ASME boilers and pressure vessel code (2019).
41. F. Alamolhoda, A. Shamiri, M. A. Hussain, R. Zarghami, R. Sotudeh-Gharebagh and N. Mostoufi, *Int. J. Chem. React. Eng.*, **17**, 20180036 (2019).
42. E. Bumrungthaichaichan, *Powder Technol.*, **396**, 327 (2022).
43. Y. A. Cengel and J. M. Cimbala, *Fluid mechanics: Fundamentals and applications*, McGraw-Hill, New York (2006).
44. S. K. Shukla, P. Shukla and P. Ghosh, *Adv. Powder Technol.*, **22**, 209 (2011).
45. A. C. Hoffmann, M. de Groot, W. Peng, H. W. A. Dries and J. Kater, *AIChE J.*, **47**, 2452 (2001).
46. P. J. Roache, *AIAA J.*, **36**, 696 (1998).
47. Z. Zhang, S. Dong, R. Jin, K. Dong, L. a. Hou and B. Wang, *Powder Technol.*, **404**, 117370 (2022).
48. B. Zhao, *Chem. Eng. Process.*, **44**, 447 (2005).
49. R. Guizani, H. Mhiri and P. Bournot, *Powder Technol.*, **314**, 599 (2017).
50. C. Galletti, A. Rum, V. Turchi and C. Nicolella, *Adv. Powder Technol.*, **31**, 1264 (2020).
51. W. Kraipech, W. Chen, F. J. Parma and T. Dyakowski, *Int. J. Min. Proc.*, **66**, 49 (2002).
52. L. Minkov, J. Dueck and T. Neesse, *Miner. Eng.*, **62**, 19 (2014).
53. B. Wang and A. B. Yu, *AIChE J.*, **56**, 1703 (2010).